Theoretical analysis of electronic band structure of 2- to 3-nm Si nanocrystals

Prokop Hapala,* Kateřina Kůsová, Ivan Pelant, and Pavel Jelínek
Institute of Physics, Academy of Sciences of the Czech Republic, v.v.i., Cukrovarnická 10, 162 00 Prague, Czech Republic
(Received 30 January 2013; published 10 May 2013)

In this paper, we discuss the validity of the band structure concept in silicon nanocrystals a few nanometers in size. We introduce a general method which allows reconstruction of a fuzzy electronic band structure of nanocrystals from ordinary real-space electronic structure calculations. A comprehensive study of the fuzzy band structure of a realistic nanocrystal is given including full geometric and electronic relaxation with the surface passivating groups. In particular, we combine this method with large-scale density functional theory calculations to obtain insight into the luminescence properties of silicon nanocrystals up to 3 nm in size depending on the surface passivation and geometric distortion. We conclude that the band-structure concept is applicable to silicon nanocrystals with a diameter larger than ≈2 nm with certain limitations. We also show how perturbations due to polarized surface groups or geometric distortion can lead to considerable moderation of momentum space selection rules.

DOI: 10.1103/PhysRevB.87.195420 PACS number(s): 73.21.La, 78.67.Hc

I. INTRODUCTION

Crystalline nanostructures are often viewed as "artificial atoms" or "zero-dimensional systems" despite being the size of a smaller protein. This is because when single nanocrystals (NCs) are experimentally probed, very sharp optical radiative transitions, implying the existence of discrete energy levels rather than energy bands, are observed.[1] On the other hand, nanostructures are known to retain some of the band-structure-related properties of their bulk counterparts, e.g., direct-band-gap semiconductor NCs such as CdSe are excellent light emitters. The concept of band structure in NCs is frequently used, because it allows one to transfer the already thoroughly studied electronic properties and the whole framework of solid-state physics of bulk materials to the nanoscale.

This brings about an apparent dichotomy and raises the question if, and under what circumstances, the band-structure concept can be applied to NCs and, moreover, if the band-structure description can overlap with the description based on discrete energy levels. In this article, we discuss a connection between the bulk band structure and molecular orbitals (MOs) of nanoparticles obtained from density functional theory (DFT) calculation using Fourier transform. Application of this method shows **k** dependence of electronic energy levels in Si NCs, a fuzzy electronic band structure, even though, strictly speaking, **k** is a good quantum number only in an ideal infinite crystal.

In indirect-band-gap semiconductors, the comprehension of the electronic band-structure behavior allows for efficient band engineering. A prime example illustrating the usefulness of the band-structure approach is germanium, an originally indirect-band-gap material successfully transformed to a direct-band-gap one by heavy doping and tensile strain.[2] This experimental realization of direct-gap bulk germanium was based on theoretical band-structure calculations.[3] What is important, however, is that the same concept was experimentally realized also in germanium NCs.[4] This example confirms that the parallels between bulk and nanocrystalline materials do exist and that they can be beneficial in material engineering as well as for the intuitive understanding of the material's behavior.

Silicon as a material found wide applications in electronics and it is still the subject of intense research. Nevertheless, the indirect-band-gap nature of the band structure of bulk silicon has always been the major obstacle for its employment in light-emitting devices since momentum conservation requires additional momentum transfer mechanisms involved in the light emission processes. The situation changed dramatically in the last two decades due to the emergence of the possibility of preparing Si-based structures of nanometer size, where quantum effects begin to play a dominant role. In particular, great effort has been devoted to the study of the optical properties of Si NCs in recent years, with a perspective of potential for real-life applications such as, e.g., light emitting diodes, next-generation solar cells, and biomedical devices.[5–8] The discovery of efficient visible photoluminescence[9] and optical gain[10] from silicon NCs has demonstrated the possibility of partially overcoming the limitations of the indirect band gap of silicon by exploiting the quantum phenomena at the nanoscale. Despite the large amount of papers published on this subject, there are still many aspects which are not fully understood and are the subject of intense dispute.

As already mentioned, the theoretical concept of optical properties of Si NCs is often discussed in the framework of the band-structure picture of the bulk material. However, the finite size of a system measuring only a few nanometers makes the justification of this approach questionable. Therefore, the validity of the band-structure concept and, if need be, its character in Si NCs of a given size and surface passivation have to be analyzed.

Traditional electronic structure calculations of Si NCs, treated as a finite system, provide *a priori* only real-space MOs, where the crystal momentum and thus the fuzzy band structure $E(\mathbf{k})$ are not directly accessible. What is more, in NCs with typical sizes of a few nanometers, the surface-to-volume ratio substantially increases and thus the interface between the NCs and their environment plays a crucial role in tailoring their optical properties. Consequently, the optoelectronic properties of Si NCs are very sensitive to their surface passivation, symmetry, and applied strain, which makes the application of simple (bulk-like) models questionable.

Several attempts (see, e.g., Refs. 11–16) have been made to perform the projection of states of finite systems from real to reciprocal space, and vice versa. However, to the best of our knowledge, a detailed analysis of the fuzzy electron band structure of fully relaxed Si NCs on DFT level has been missing so far. Therefore, a robust method which allows band-structure mapping from fully relaxed DFT calculations of realistic Si NCs is required.

From the perspective of theoretical simulations, many approaches, ranging from parametrized semiempirical methods such as pseudopotential,[17,18] $\mathbf{k}\cdot\mathbf{p}$,[19] and tight binding[11,20–24] to *ab initio* methods,[25–30] have been adopted to investigate the optical and electronic properties of Si nanocrystalline structures. Semiemperical methods based on the parametrization of the bulk band structure might provide a good description of some properties (e.g., band gaps, exciton binding energies, and radiative transition rates) often beyond the accuracy of *ab initio* methods like DFT-LDA. What is more, semiempirical methods are also less computationally demanding, which enables one to handle Si NCs of a realistic size consisting of tens of thousands of atoms. On the other hand, the transferability of semiempirical methods is limited when pronounced atomic relaxation or charge transfer within NCs occurs, e.g., due to different surface passivation. Here *ab initio* methods provide an accurate description of electronic states of fully relaxed Si NCs, but simulations of realistic systems of nanometer size are impossible due to excessive computational demand. From this point of view, the application of fast local orbital DFT codes[31] seems to be the optimal choice.

In this paper, we introduce a general method which allows reconstruction of the fuzzy band structure from MOs obtained, e.g., from *ab initio* calculations. For this reason, we dare to use the terms highest occupied molecular orbital (HOMO) and lowest unoccupied molecular orbital (LUMO) and valence-band maximum/conduction-band minimum as synonyms throughout this article. We demonstrate the method's capability of folding up the fuzzy band structure of finite systems in a simple one-dimensional (1D) atomic chain consisting of a few H atoms. Using this example, we discuss the main characteristic features of the fuzzy band structure of finite-size systems. Next, we apply the procedure to the analysis of the electronic structure of freestanding Si NCs obtained from DFT calculations. To achieve this objective, we adopt the fast local orbital DFT code FIREBALL[31,32] devised with the aim of achieving computational efficiency but still providing the desired precision in the description of the ground-state electronic structure. This allows us to perform fully relaxed total energy calculations of different Si NCs consisting of up to a thousand atoms in a feasible way. We show how the fuzzy electronic band structure of Si NCs is affected by their surface passivation, symmetry, and size.

II. METHODS

A. DFT calculations

All computations were carried out using the local orbital DFT code FIREBALL[31,32] within the local density approximation (LDA) for the exchange-correlation functional. Valence electrons have been described by optimized[33] numerical atomic-like orbitals having the following cutoff radii (in a.u.): Rc(s, s*) = 4.0 for H; Rc(s) = 4.5, Rc(p) = 4.5, and Rc(d) = 5.4 for C; Rc(s) = 4.8, Rc(p) = 5.4, and Rc(d) = 5.2 for Si; and Rc(s) = 3.5, Rc(p) = 4.0, and Rc(d) = 5.0 for O, respectively. The correctness of the basis set was checked to reproduce the band structure of bulk silicon within LDA accuracy.

NCs are represented by cluster models with three core sizes, consisting of 68, 232, and 538 Si atoms. These three models represent Si NCs with diameters of 1.5, 2.0, and 2.5 nm, respectively (Fig. 1). The atomic structure of the Si_{538} core was cut out from a relaxed bulk silicon lattice in a way so as to minimize the number of unsaturated bonds and to reflect the lattice symmetry with well-defined (111) and (100) faces (Fig. 1). Subsequently, the smaller Si_{232} and Si_{68} cores were derived from Si_{538} by removing the topmost atomic layer, in order to get a smaller analog of the same symmetry and surface faces. Here index numbers stand for the number of Si atoms forming the NC core. The Si core of each of the three models is terminated with either polar (–OH, simulating an oxidized layer) or nonpolar (–H, $–CH_3$) passivating groups, leaving all surface Si atoms fully saturated. Therefore, the total number of atoms in nanoparticles varies from several hundred up to more then 1400 for a Si_{538} nanoparticle capped with a methyl group, $–CH_3$.

All Si NCs models were fully optimized, allowing the relaxation of all atoms. Total energy calculations were performed as a cluster calculation ($\mathbf{k} = 0$) and the convergence was achieved when a residual total energy of 0.0001 eV and a maximal force of 0.05 eV/Å were reached.

B. Momentum-space projection of molecular orbitals

The band-structure theory of solids is well established and it has been successfully applied to real materials to explain their physical and material properties, e.g., electrical resistivity and optical absorption. A cornerstone of the band-structure theory is the so-called Bloch's theorem,[34] which initiated the epoch of modern solid-state physics. Electronic states in an infinite periodic system are described via the Schrödinger equation,

$$[\nabla^2 + V(\mathbf{r})]\Psi(\mathbf{r}) = \epsilon\Psi(\mathbf{r}), \tag{1}$$

where ϵ is the energy of eigenstate $\Psi(\mathbf{r})$ and potential $V(\mathbf{r})$ is periodic $V(\mathbf{r}) = V(\mathbf{r}+\mathbf{R})$, $\mathbf{R}$ being the translational lattice vector. Bloch's theorem postulates that the solution of the Schrödinger equation, $\Psi_{n,\mathbf{k}}(\mathbf{r})$, can be written as the product of a real mother function $u_{n,\mathbf{k}}(\mathbf{r})$, which is also periodic, $u_{n,\mathbf{k}}(\mathbf{r}) = u_{n,\mathbf{k}}(\mathbf{r}+\mathbf{R})$, and a Bloch plane wave, $e^{i\mathbf{k}.\mathbf{r}}$:

$$\Psi_{n,\mathbf{k}}(\mathbf{r}) = u_{n,\mathbf{k}}(\mathbf{r}).e^{i\mathbf{k}.\mathbf{r}}. \tag{2}$$

The eigenstate $\Psi_{n,\mathbf{k}}(\mathbf{r})$ varies continuously with the wave vector $\mathbf{k}$ and forms an energy band $\epsilon_{n,\mathbf{k}}$ identified by the band index n.

How does the band-structure picture change when the size of the system is reduced? Or, in other words, is the concept of energy bands also valid for nanoscopic systems? As we show in the following, the finite size of a system has two important consequences: (i) wave vector $\mathbf{k}$ becomes discrete, and (ii) wave functions are delocalized in momentum space.[35]

The first statement, i, directly follows from the construction of reciprocal space. For example, let us assume a 1D

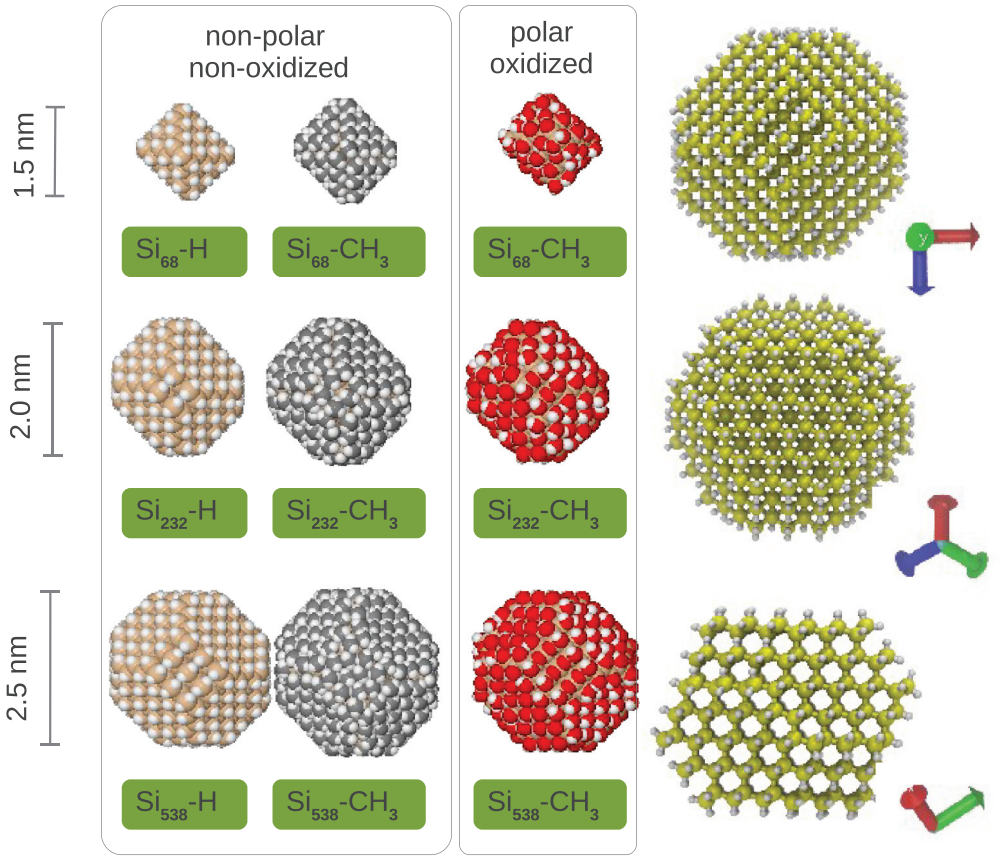

FIG. 1. (Color online) Geometry of model nanocrystals. The first two panels show nine models of NCs of three core sizes (68, 232, and 538 Si atoms of diameter 1.5, 2.0, and 2.5 nm) with either polar oxidized (–OH) or nonpolar (–H, $–CH_3$) passivation. The last panel shows the geometry of Si_{538}-H from the important crystallographic directions (100), (111), and perpendicular to (111).

monoatomic chain of N atoms with the lattice constant a. There are N different wave vectors $\mathbf{k}$ separated by

$$\Delta k^{(1)} = \frac{2\pi}{aN} = \frac{2\pi}{L}, \tag{3}$$

where $L = Na$ is the length of the chain. Obviously, if N becomes small, the separation between the wave vectors $\Delta k^{(1)}$ becomes larger.

The second statement, ii, says that, according to the Heisenberg uncertainty principle, the crystal momentum becomes delocalized as follows:

$$\Delta x \Delta p > h. \tag{4}$$

Substituting the crystal momentum $p = \frac{h}{2\pi}k$ and the size of the NC $\Delta x = L$ into the equation above, we obtain the relation for the delocalization of the wave vector due to the finite size of the system:

$$\Delta k^{(2)} > \frac{2\pi}{L}. \tag{5}$$

The fact that the separation of discretized wave vectors $\Delta k^{(1)}$ and their delocalization $\Delta k^{(2)}$ are of the same order calls for a more rigorous discussion of the band structure of finite systems, which is provided in the following text. We use natural units ($\hbar = 1$), using $\mathbf{k}$ as a synonym for momentum. To simulate the finite size of systems (e.g., an NC) we introduce the so-called window function $w(\mathbf{r})$, which restricts the wave function $\Psi_{n,\mathbf{k}}(\mathbf{r})$ to the space occupied by the system. Then Eq. (2) is modified accordingly:

$$\Psi_{n,\mathbf{k}}(\mathbf{r}) = w(\mathbf{r})u_{n,\mathbf{k}}(\mathbf{r}).\mathrm{e}^{i\mathbf{k}.\mathbf{r}}. \tag{6}$$

Figure 2 depicts the characteristics of the individual terms in Eq. (6) in a 1D case. We should note that the concept of the window function is similar to an envelope function used in the frame of the $\mathbf{k}\cdot\mathbf{p}$ method (see, e.g., Ref. 19 for more details). In the simplest approximation, one can define the window function $w(\mathbf{r})$ as a stepwise function,

$$w(x) = \begin{cases} 1 & : \quad |\mathbf{r}| < L, \\ 0 & : \quad |\mathbf{r}| > L, \end{cases} \tag{7}$$

which vanishes outside the NC [see Fig. 2(a)]. Then the resulting real-space wave function $\Psi_{n,\mathbf{k}}(\mathbf{r})$ consists of the modulation of the mother function by the Bloch plane wave and the window function $w(\mathbf{r})$ [see Fig. 2(d)]. In real systems, the window function can have a more complicated shape dictated by the electronic structure of a particular system [see dashed (green) line in Fig. 2(a)].

Let us consider a problem inverse to the computation of the band structure from Bloch's theorem [Fig. 3(a)]. We know the real-space wave function $\phi_i(\mathbf{r})$ of the ith eigenstate (e.g., a Kohn-Sham MO obtained from an aperiodic DFT calculation of a nanoscopic system), and we would like to assign the corresponding crystal momentum $\mathbf{k}$. Each MO of energy ϵ_i

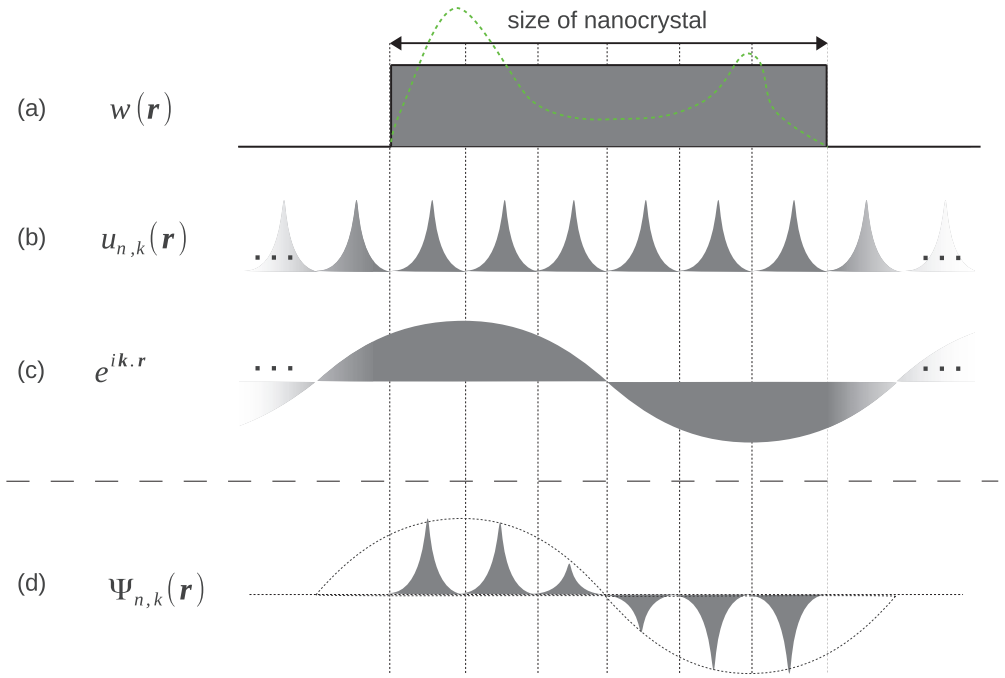

FIG. 2. (Color online) Schematic illustration of Eq. (6). (a) Window function constraining the wave function to a finite area of space. In general, it is the envelope of an MO and it can have a complicated shape [dashed (green) line]. However, for simplicity, we expect the rectangular shape of Eq. (7) (gray rectangle). (b) Mother function of an infinite system composed of a linear combination of atomic orbitals. (c) Infinite Bloch plane wave. (d) Final wave function of a nanocrystal as a product of (a), (b), and (c) constrained in a finite area of space.

can cross one or more bands $\epsilon_{n,\mathbf{k}}$ [Fig. 3(b)]. Then we can assume the MO $\phi_i(\mathbf{r})$ to be a linear combination of A bands $\Psi_{n,\mathbf{k}}(\mathbf{r})$,

$$\phi_i(\mathbf{r}) = \sum_{a=0}^{A} d_a \Psi_{n_a,\mathbf{k}_a}(\mathbf{r}), \tag{8}$$

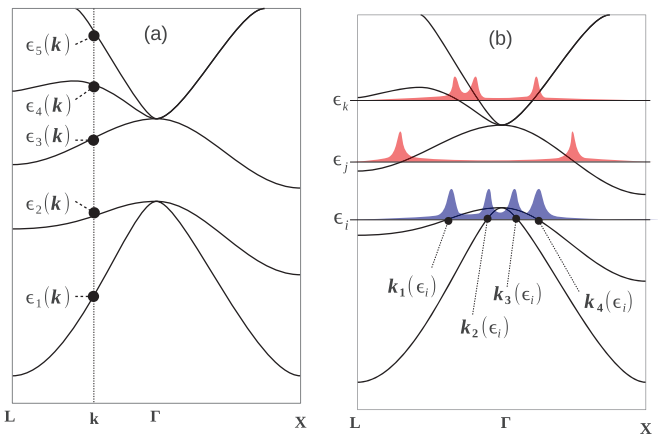

FIG. 3. (Color online) Schematic of Eq. (8). (a) Usual approach to obtaining the band structure of an infinite crystal using Bloch's theorem. For a given $\mathbf{k}$ vector, the energy spectrum of $\epsilon_{n,\mathbf{k}}$ is found. (b) Inverse approach in a finite system. For a given energy state ϵ_i of orbital ϕ_i, the corresponding $\mathbf{k}$ vectors need to be found. The orbital is a linear combination of all Bloch-like wave functions $\Psi_{n,\mathbf{k}}(\mathbf{r})$ corresponding to the $n,\mathbf{k}$ in which the orbital energy ϵ_i crosses the energy bands $\epsilon_n(\mathbf{k})$.

where, for a particular $\phi_i(\mathbf{r})$, neither the indexes $n_a,\mathbf{k}_a$ nor the coefficients d_a are explicitly known.

One option for extracting $\mathbf{k}$ vectors of $\phi_i(\mathbf{r})$ lies in the determination of the corresponding $\Psi_{n_a,\mathbf{k}_a}(\mathbf{r})$ and $u_{n_a,\mathbf{k}_a}(\mathbf{r})$ and the consecutive extraction of the Bloch factor $e^{i\mathbf{k}.\mathbf{r}}$ from Eq. (6). This is possible, for example, by projecting $\phi_i(\mathbf{r})$ on $\Psi^{\mathrm{BULK}}_{n,\mathbf{k}}(\mathbf{r})$ obtained from the bulk calculation.[13] Nevertheless, wave functions $\Psi_{n,\mathbf{k}}(\mathbf{r})$ in a finite system may differ considerably from the bulk one $\Psi^{\mathrm{BULK}}_{n,\mathbf{k}}(\mathbf{r})$ [e.g., if $w(\mathbf{r})$ is more complicated], and a large number of states have to be considered for a large NC. These complications hamper a robust implementation of this method to a computational code.

Here we opt for another method, which transforms MO $\phi_i(\mathbf{r})$ from real into reciprocal space using Fourier transform. A similar approach was successfully applied to analyze angular resolved photoemission (ARPES) spectra of oligomeric organic molecules.[12] In our scheme, a selected $\phi_i(\mathbf{r})$ expanded on a real-space grid is projected to momentum space either using discrete 3D fast Fourier transform (FFT) or by the projection onto a set of plane waves $e^{i\mathbf{k}'.\mathbf{r}}$,

$$\tilde{\phi}_i(\mathbf{k}') = \langle \phi_i(\mathbf{r}) | e^{i\mathbf{k}'.\mathbf{r}} \rangle, \tag{9}$$

where $\mathbf{k}'$ is an arbitrary wave vector.

For practical use, we plot the so-called momentum density $\tilde{\rho}_i(\mathbf{k}')$, which is real, instead of the complex Fourier transform $\tilde{\phi}_i(\mathbf{k}')$. The momentum density $\tilde{\rho}_i(\mathbf{k}')$ can be written, using Eq. (9), as follows:

$$\tilde{\rho}_i(\mathbf{k}') = |\tilde{\phi}_i(\mathbf{k}')|^2. \tag{10}$$

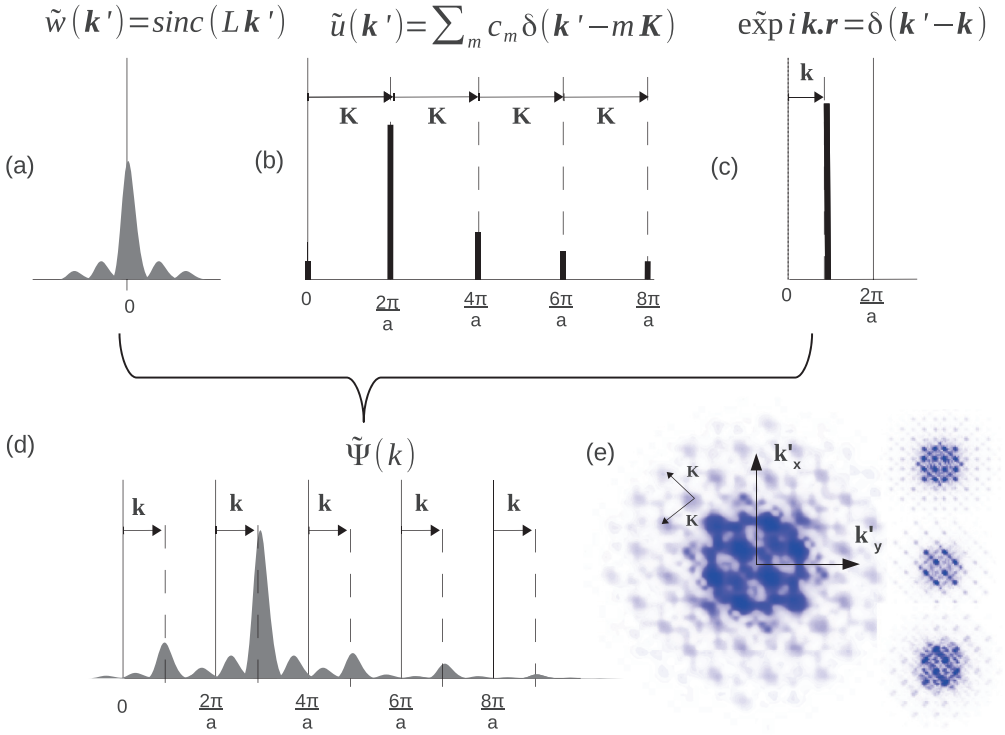

FIG. 4. (Color online) Schematic of convolution of momentum-space representations of the three wave-function components. (a) Rectangular window function transformed to sinc($L\mathbf{k}'$). (b) Bulk-like mother function transformed to a series of δ functions in the centers of Brillouin zones. (c) Bloch wave transformed to a δ function inside the first Brillouin zone shifted out of the center. (d) Momentum-space representation of the wave function created by the convolution of (a), (b), and (c) in a 1D case. (e) Illustration of a higher-dimensional case: a 2D view of the momentum-space density of MOs in a silicon nanocrystal. Note the side artifacts spaced by multiples of K representing the higher Fourier components c_m in the expansion of the mother function.

It also contains the information about the delocalization of the MO in momentum space and it can be plotted as a function of wave vector along a selected line in momentum space [see Fig. 4(d)].

The first approach (FFT) provides a picture of the 3D structure and symmetries of the particular state in reciprocal space [see Fig. 4(e). Nevertheless, its resolution is limited by the size of the real-space grid on which MOs are expanded. The second approach (the projection on the set of plane waves) is more suitable for sticking with the traditional 1D band-structure representation plotted along the lines connecting the high-symmetry points in $\mathbf{k}$ space. In this case, we let $\mathbf{k}'$ sample the given high-symmetry line in $\mathbf{k}$ space with a much higher resolution. Although this approach is straightforward, a rigorous analysis of the structure of the resulting momentum-space distribution is required. For simplicity, let us assume a one-to-one correspondence between a particular MO and a band wave function $\phi_i(\mathbf{r}) = \Psi_{n,\mathbf{k}}(\mathbf{r})$. Note that the generalization of the following discussion if $\phi_i(\mathbf{r})$ is a linear combination of several $\Psi_{n_a,\mathbf{k}_a}(\mathbf{r})$, Eq. (8), is straightforward due to the linearity of Fourier transform. Fourier transform of a wave function $\Psi_{n,\mathbf{k}}(\mathbf{r})$ given by Eq. (6) can be expressed as a convolution of the three terms:

$$\tilde{\Psi}_{n,\mathbf{k}}(\mathbf{k}') = \tilde{w}(\mathbf{k}') * \tilde{u}(\mathbf{k}') * \delta(\mathbf{k}' - \mathbf{k}). \tag{11}$$

It is well worth analyzing in detail the process of convolution and the character of each term in Eq. (11). To make our discussion more illustrative, we restrict ourselves to the 1D case. Figure 4 represents schematically the process of convolution and the character of each term separately.

We start from the trivial third term. $\delta(\mathbf{k}' - \mathbf{k})$ is a Fourier transform of Bloch wave $e^{i\mathbf{k}.\mathbf{r}}$, where $\mathbf{k}$ is from the first Brillouin zone [see Fig. 4(c)] and attains some of the discrete values separated by $\Delta k^{(1)} = 2\pi/L$ as postulated in Eq. (3).

The first term in $\tilde{w}(\mathbf{k}')$ in Eq. (11) is a Fourier image of the window function $w(\mathbf{r})$. This term causes the delocalization of wave function in $\mathbf{k}$ space. Considering the window function $w(\mathbf{r})$ as the step function of length L [see Eq. (7)], its Fourier transform equals $\tilde{w}(\mathbf{k}') = \mathrm{sinc}(L\mathbf{k}')$. Using Eq. (5), it can be expressed also as $\mathrm{sinc}(2\pi\mathbf{k}'/\Delta k^{(2)})$, which brings us back to the Heisenberg principle.

The square $|\tilde{w}(\mathbf{k}')|^2$ introduces to the momentum-space density $\tilde{\rho}_i(\mathbf{k}')$ a blur with a Lorentzian envelope [see Eq. 4(a)] of slow asymptotic decay $1/(L\mathbf{k}')^2$. This has an important implication for the momentum selection rules for the transitions between states in finite systems: two wave functions centered around different $\mathbf{k}$ can have non-negligible overlap in $\mathbf{k}$ space even if their separation in $\mathbf{k}$ is fairly large.

We would like to stress that the decay in the momentum-space projection depends strongly on the actual shape of $w(\mathbf{r})$. Therefore, this approach is superior to a simple estimation of momentum uncertainty based on the Heisenberg principle, which can provide only the width of the peak around $\mathbf{k}$, and says nothing about its decay.

Finally, the second term in Eq. (11), $\tilde{u}(\mathbf{k}')$, corresponds to the Fourier transform of the mother function $u_{n,\mathbf{k}}(\mathbf{r})$, which

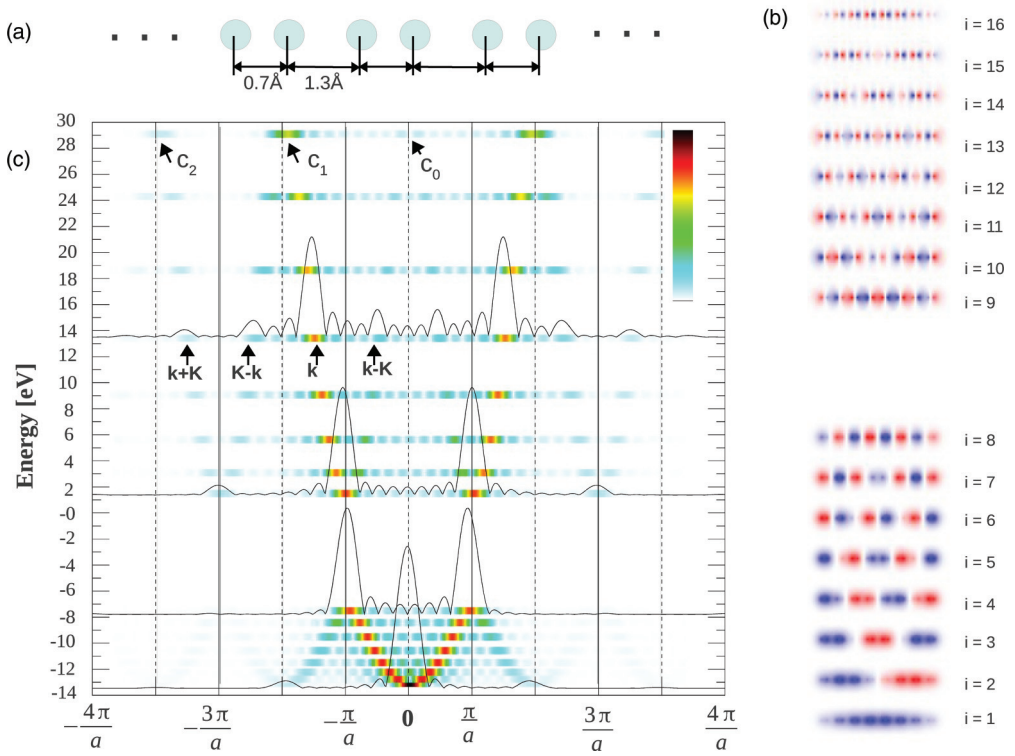

FIG. 5. (Color online) One-dimensional cross section of momentum-space projected MOs of a chain of eight hydrogen molecules. (a) Atomic structure of a molecular hydrogen chain with bond lengths of 0.7 Å electronically coupled through the intermolecular distance of 1.3 Å. (b) Real-space projection of MOs $\phi_i(\mathbf{r})$ of the system. The first eight orbitals are bonding and occupied; the remaining eight are antibonding and unoccupied. The positive sign of the wave function is shown in blue; the negative sign, in red. (c) Band structure of the finite chain as assembled from momentum densities $\rho_i(\mathbf{k}')$ plotted at a particular orbital energy ϵ_i by color scale. Parabolic band dispersion can be clearly seen following the maxima of densities (yellow-red-black). For some of the orbitals $i = 1, 8, 9, 13$, the actual shape of function $\rho_i(\mathbf{k}')$ is also plotted to illustrate the correspondence to Fig. 4. The main peaks corresponding to the Fourier components in the expansion of $u_{n,\mathbf{k}}(\mathbf{k}')$ are denoted by arrows.

can be expanded in a discrete Fourier series of waves using its periodicity,

$$u_{n,\mathbf{k}}(\mathbf{r}) = \sum_{m=0}^{\infty} c_m e^{i(m.\mathbf{K}).\mathbf{r}}, \tag{12}$$

where $\mathbf{K}$ denotes the reciprocal lattice vector and m is an integer index addressing different reciprocal unit cells. This expression is transformed to reciprocal space as

$$\tilde{u}_{n,\mathbf{k}}(\mathbf{k}') = \left\langle \sum_{m=0}^{\infty} c_m e^{i(m.\mathbf{K}).\mathbf{r}} \middle| e^{i\mathbf{k}'.\mathbf{r}} \right\rangle = \sum_{m=0}^{\infty} c_m \delta(\mathbf{k}' - m.\mathbf{K}), \tag{13}$$

where $\delta(\mathbf{k}' - m.\mathbf{K})$ is situated in the center of the mth reciprocal unit cell (i.e., not in the first Brillouin zone).

Typically, $u_{n,\mathbf{k}}(\mathbf{r})$ is relatively smooth in the unit cell and so the Fourier expansion coefficients c_m decay with increasing frequency [Fig. 4(b)]. In reality, just one expansion coefficient is dominant. The dominant Fourier component is determined by the nodal structure of $u_{n,\mathbf{k}}(\mathbf{r})$, where nodes are introduced either by the antibonding character of the mother function or by the contribution of the higher angular momentum atomic orbitals (such as a p orbital). If $u_{n,\mathbf{k}}(\mathbf{r})$ has no node inside a unit cell (for example, the bonding state of two s orbitals), the first coefficient c_0 situated in the center of the first Brillouin zone ($\mathbf{k}' = 0$) is the dominant term. Similarly, if $u_{n,\mathbf{k}}(\mathbf{r})$ has m nodes, the mth Fourier expansion coefficient c_m dominates. This means that most of the momentum-space density is situated in the mth reciprocal unit cell. Consequently, the convolution of $\tilde{u}_{n,\mathbf{k}}(\mathbf{k}')$ with the Bloch term $\delta(\mathbf{k}' - \mathbf{k})$ forms a new band located in the mth reciprocal unit cell [see the antibonding band in Fig. 5(c). Thus, our approach provides the reconstruction of the so-called *unfolded* band structure, where each band is situated in a different reciprocal unit cell. Note also that in the 3D case the index m is a vector, and nodes in each dimension should be considered independently.

Now we illustrate the projection method in a simple case. Let us analyze the electronic structure of a finite 1D chain consisting of eight coupled hydrogen molecules (see Fig. 5), where the unit cell consists of a single hydrogen molecule. Upon projecting real-space MOs [Fig. 5(b)] into $\mathbf{k}$ space two distinct bands isolated by a bandgap appear [see Fig. 5(c)]. The lower band ($m = 0$), composed of bonding orbitals with no node inside the unit cell, has the dominant Fourier components located in the first Brillouin zone. The higher antibonding band ($m = 1$) has the dominant Fourier components located in the second reciprocal unit cell.

Apart from these dominant Fourier components, which characterize the band structure, there are also smaller satellite peaks representing the other components c_m in the Fourier

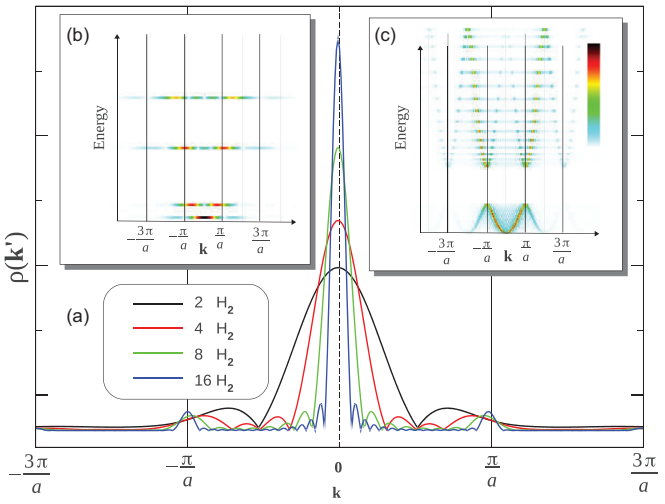

FIG. 6. (Color online) Dependence of the delocalization of momentum density $\tilde{\rho}_i(\mathbf{k}')$ of MOs in a chain of hydrogen molecules on the chain length. (a) Momentum-space delocalization of the lowest MO ($i = 1$) in chains composed of 2 (black), 4 (red), 8 (green), and 16 (blue) hydrogen molecules. (b) Band structure of a chain composed of two hydrogen molecules. (c) Fuzzy band structure of a chain composed of 16 hydrogen molecules.

expansion of $\tilde{u}_{n,\mathbf{k}}(\mathbf{k}')$. In the special case where Bloch $\mathbf{k} = 0$, the peaks are located directly in centers of the mth reciprocal unit cell and correspond directly to components c_m in the Fourier expansion of $\tilde{u}_{n,\mathbf{k}}(\mathbf{k}')$ [Eq. (13)]. This is illustrated for MO $i = 16$ by peaks denoted c_0, c_1, and c_2 in Fig. 5(c). In the general case ($\mathbf{k} \neq 0$) these peaks are split and shifted by $\pm\mathbf{k}$ as denoted by $\mathbf{K} + \mathbf{k}$ and $\mathbf{K} - \mathbf{k}$ in Fig. 5(c).

To illustrate the delocalization of the momentum vector $\mathbf{k}$ due to the finite size of the system, represented by $w(\mathbf{r})$, we analyzed the lowest band ($i = 1$) of several different 1D hydrogen chains with lengths of from 2 to 16 molecules. In Fig. 6(a) the peak width of the depicted momentum density decreases proportionally to the number of molecules (unit cells) in the chain according to Eq. (5). In this particular case, the window function $w(\mathbf{r})$ is very close to a rectangular step function. Hence, the shape of the momentum-space density $\tilde{\rho}(\mathbf{k}')$ is very similar to $|\mathrm{sinc}(L\mathbf{k}')|^2$. The frequency of this sinc-like function can be also deduced from the number of nodes per reciprocal unit cell, which is proportional to the increasing chain length L.

Let us summarize the main conclusions of this section. We have discussed two main implications of the finite size of an NC for its band structure: (i) the discretization and (ii) the delocalization of wave vector $\mathbf{k}$. We have introduced a robust method of projection of MOs to $\mathbf{k}$ space, which provides the band structure of a finite system and discussed in detail the analysis of the resulting momentum densities $\tilde{\rho}_i(\mathbf{k}')$. We have demonstrated that the important characteristics (i.e., the Bloch $\mathbf{k}$ vector, its delocalization, and the discrimination

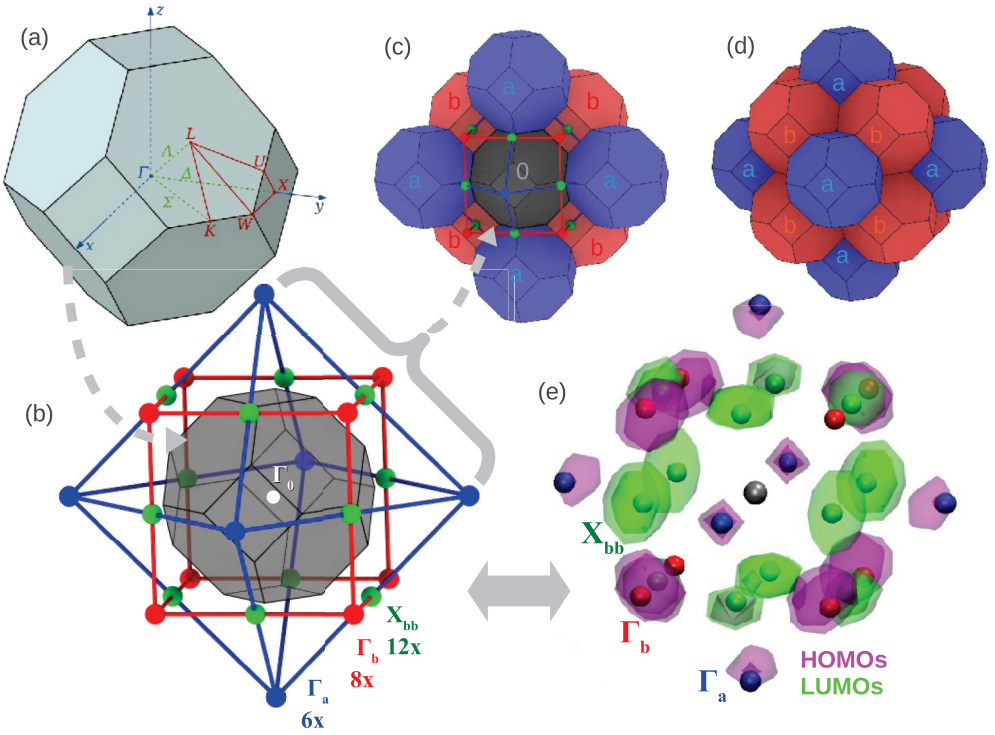

FIG. 7. (Color online) Three-dimensional structure of a silicon reciprocal lattice. (a) Structure of the first Brillouin zone of silicon in the shape of a truncated octahedron with high symmetry directions shown. (b) Positions of points Γ_a (blue), Γ_b (red), and X_{bb} (green) around the first Brillouin zone. (c) Points Γ_a, Γ_b, and X_{bb} in the context of sublattices **a** (blue) and **b** (red). (d) Reciprocal unit cells adjacent to the first Brillouin zone, distinguished by sublattices **a** (blue) and **b** (red). (e) Three-dimensional view of the localization of the maximal $\mathbf{k}$ space projected density of HOMOs (green) and LUMOs (purple) for a Si_{68}-H NC. Points Γ_a, Γ_b, and X_{bb} are marked by spheres to highlight the correspondence.

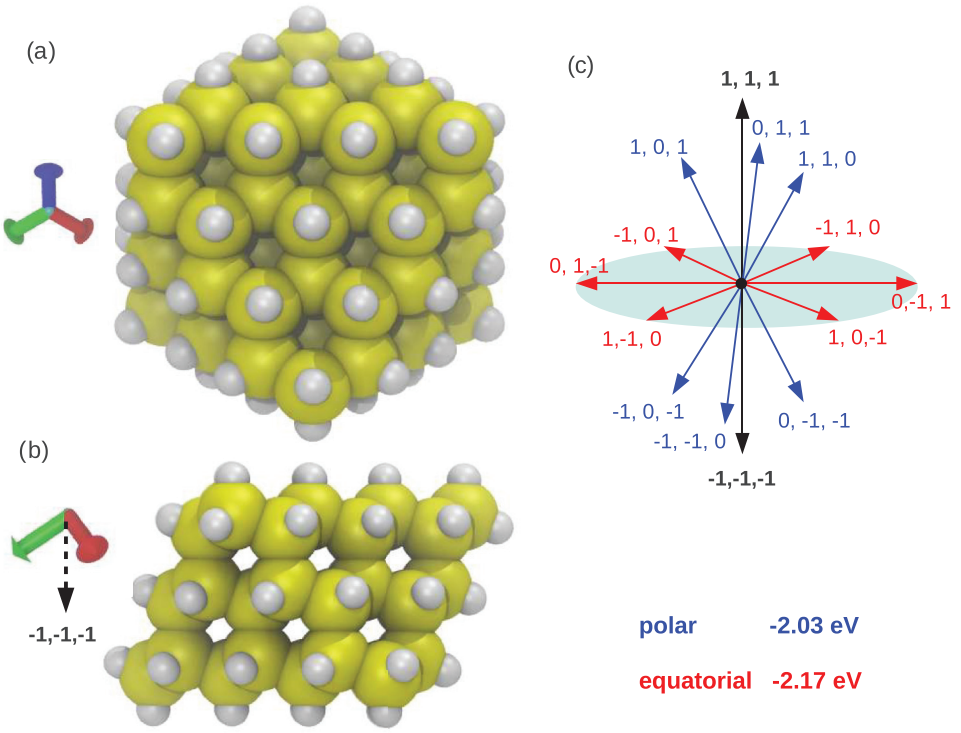

FIG. 8. (Color online) Degeneracy loss due to the broken symmetry of a Si_{68}-H nanocrystal. (a) Top view of a Si_{68}-H nanocrystal along the 111 direction. (b) Side view of a Si_{68}-H nanocrystal perpendicular to the 111 direction. (c) Two classes of energy split MOs of Si_{68}-H due to anisotropic confinement. There are six degenerate states in directions closer to the 111 direction [polar (blue)] with an energy of 2.17 eV and another six degenerate states more perpendicular to the 111 direction with an energy of −2.03 eV [equatorial (red)]. Note that states **k** and −**k** are always degenerate due to time-reversal symmetry and the realness of the wave function in a finite system.

of independent bands) can be extracted from the resulting momentum densities, despite the convolution in Eq. (11).

C. Band structure of bulk silicon and nanocrystal

Before we advance from the 1D hydrogen chain to the band structure of a silicon NC, it is worth discussing in detail the reciprocal space structure of bulk silicon. While in solid-state physics it is common to describe band structure in the compact picture (or reduced-zone scheme), where all bands are folded into the first Brillouin zone, for our purposes it is more suitable to use the so-called unfolded picture. In this approach, bands located in higher reciprocal unit cells are considered independently.

Silicon crystallizes in a diamond lattice consisting of two interpenetrating face-centered cubic (fcc) Bravais lattices. In real space, the fcc Wigner-Seitz cells build up a rhombic icosahedral honeycomb, which converts to a truncated octahedral honeycomb in reciprocal space. As shown in Fig. 7(d), the reciprocal lattice is composed of two cubic sublattices **a** (blue) and **b** (red) with a truncated octahedral shape. Sublattice **a** is centered in Γ_0 of the first Brillouin zone and sublattice **b** is shifted by a vector (1,1,1) with respect to sublattice **a**. Thus, sublattice **b** is situated in the cube vertexes, and sublattice **a** in the cube centers of a body-centered cubic lattice (bcc), as shown in Fig. 7(b).

The unit cell located at Γ_0 is the first Brillouin zone. There are, in total, 14 reciprocal unit cells adjacent to the first Brillouin zone. Six of them belong to sublattice **a**, being centered at points Γ_a with coordinates $\forall$ (±2, 0, 0). Another eight unit cells belong to sublattice **b** centered at Γ_b with coordinates $\forall$ (±1, ±1, ±1). Here, $\forall$ means all permutations of axes and signs [e.g., (±2, 0, 0), (0, ±2, 0) and (0, 0, ±2)].

All 14 of these reciprocal unit cells are of crucial importance for us, because both the valence and the conduction bands are situated there (in the *unfolded* picture). In particular, the valence band maximum is located at points Γ_a and Γ_b. The *absolute* conduction band minimum in bulk silicon is located near points X_{bb} of coordinates $\forall$ (±1, ±1, 0), which are halfway between two Γ_b. The positions of points Γ_a, Γ_b, and X_{bb} are schematically depicted in Fig. 7(b). The localization of the maximal **k**-space projected density obtained from HOMOs (purple) and LUMOs (green) for a Si_{68}-H NCis shown in Fig. 7(e). From this figure, it is evident that HOMOs are localized at Γ_a and Γ_b, and LUMOs near the X_{bb} points. To make the context more clear, in Fig. 7(c) we also depict the positions of the important points Γ_a, Γ_b, and X_{bb} in the context of sublattices **a** and **b**. Because of convolution with Fourier expansion of the mother function [Eq. (13) or, more illustrative, Figs. 4(b) and 4(d)], both the valence and the conduction bands are situated outside of the first Brillouin zone in the unfolded picture. Therefore, the first Brillouin zone does not play any significant role in optical transitions and it is depicted in gray in Figs. 7(b) and 7(c).

In the case of bulk silicon, all these reciprocal unit cells around Γ_a and Γ_b are equivalent due to lattice symmetry.

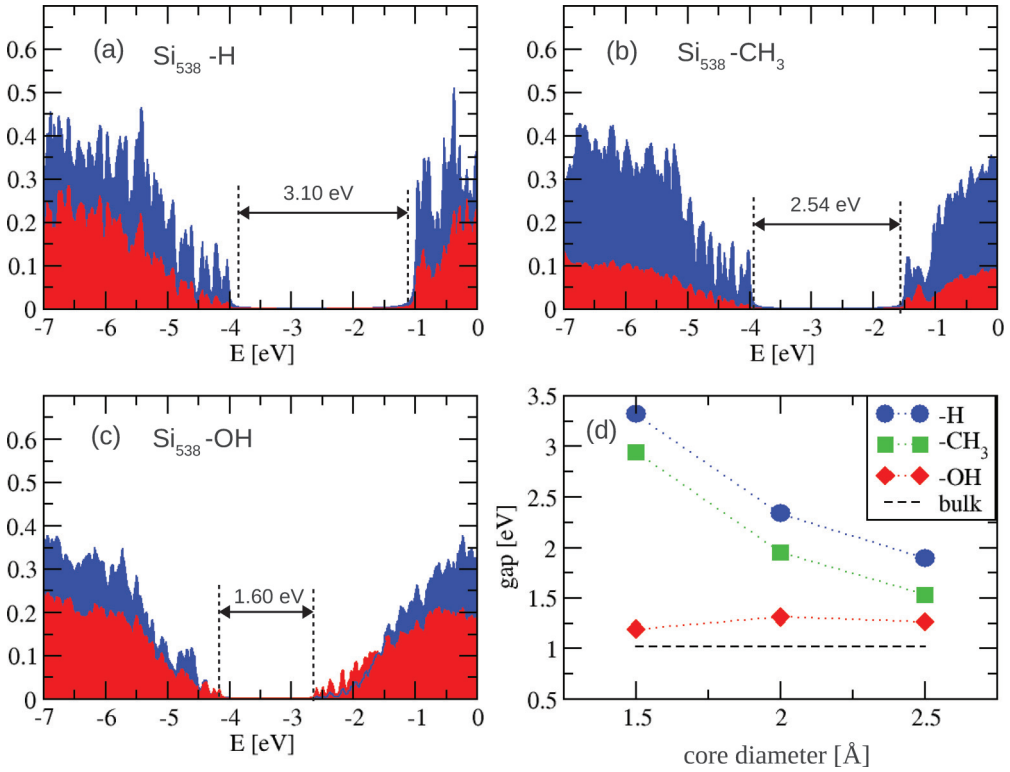

FIG. 9. (Color online) Projected density of states around a gap split into the contributions of surface (red) and core (blue) atoms, for nonpolar passivation of (a) Si_{538}-H and (b) Si_{538}-CH_3; frontier orbitals are localized mostly inside the core. However, for an oxidized NC, (c) Si_{538}-OH, these are mostly surface states. (d) Variation of energy HOMO-LUMO gap with core diameter for all three types of passivation.

Therefore also the frontier orbitals (HOMOs and LUMOs), which are composed of Bloch states located at Γ_a, Γ_b, and X_{bb}, are energetically degenerate. More precisely, HOMOs (LUMOs) are arbitrary linear combinations of Bloch states from different Γ_a and Γ_b (X_{bb}) as discussed previously [Eq. (8) and Fig. 3].

However, this is no longer true in NCs, where the symmetry is broken due to different lengths in each direction or due to anisotropic perturbations (e.g., mechanical strain) induced by surface passivation. This is another reason why it is necessary to describe the band structure of an NC in the unfolded picture with all reciprocal unit cells independent.

In other words, the anisotropy of NCs removes the degeneracy of MOs. We can observe this in our model NCs even though the shape of the cores (Si_{68}, Si_{232}, Si_{538}) respects the cubic symmetry of the silicon lattice. In the case of –H passivation, the degeneracy is almost preserved, because no anisotropic strain or electrostatic field is induced. The LUMO state is 12-fold degenerate, representing the 12 X_{bb} points.

However, due to the shape of a Si_{68}-H NC—slightly shorter in the (111) direction [Fig. 8(a)]—MOs are split into two classes of slightly different energies. Electronic states with the **k** vector oriented more closely to (111) have an energy of 2.17 eV, while states with the **k** vector oriented more perpendicularly to the (111) direction have an energy of −2.03 eV [see Fig. 8(c)].

Finally, we comment on the importance of MO symmetry for optical transitions. Since MOs are real functions, their Fourier transforms are symmetric for **k** and −**k**. Consequently, we can identify two distinct classes of MOs according to the character of their symmetry: (a) if an MO is an even function in real space, its **k**-space representation becomes real (cosine part); and (b) if an MO is an odd function, the **k**-space representation is purely imaginary (sine part). According to selection rules, optical transitions are strongest between two states localized around the same point in **k** space with a complementary symmetry character, i.e., sine to cosine, or vice versa.

III. RESULTS

It is well known that the electronic states of silicon nanoparticles at the band edge are very sensitive to surface passivation.[26,36,37] In this section, we employ the method to analyze the fuzzy band structure of Si NCs as a function of their diameter and surface passivation including both polar (–OH) and nonpolar (–H, –CH_3) groups.

A. SiNC:H

First, we consider Si NCs passivated by hydrogen groups (–H). Our calculations of the fully optimized structure show that the atomic relaxation of Si atoms in the core region is negligible. Therefore, the Si NC core has very similar atomic structure as bulk Si. We attribute this effect to (i) the negligible charge transfer between the Si core and the hydrogen terminating groups due to the fairly close electronegativities of both elements (1.9 for Si and 2.2 for H, respectively) and (ii) the absence of mechanical stress resulting from the small volume of the hydrogen terminating groups.

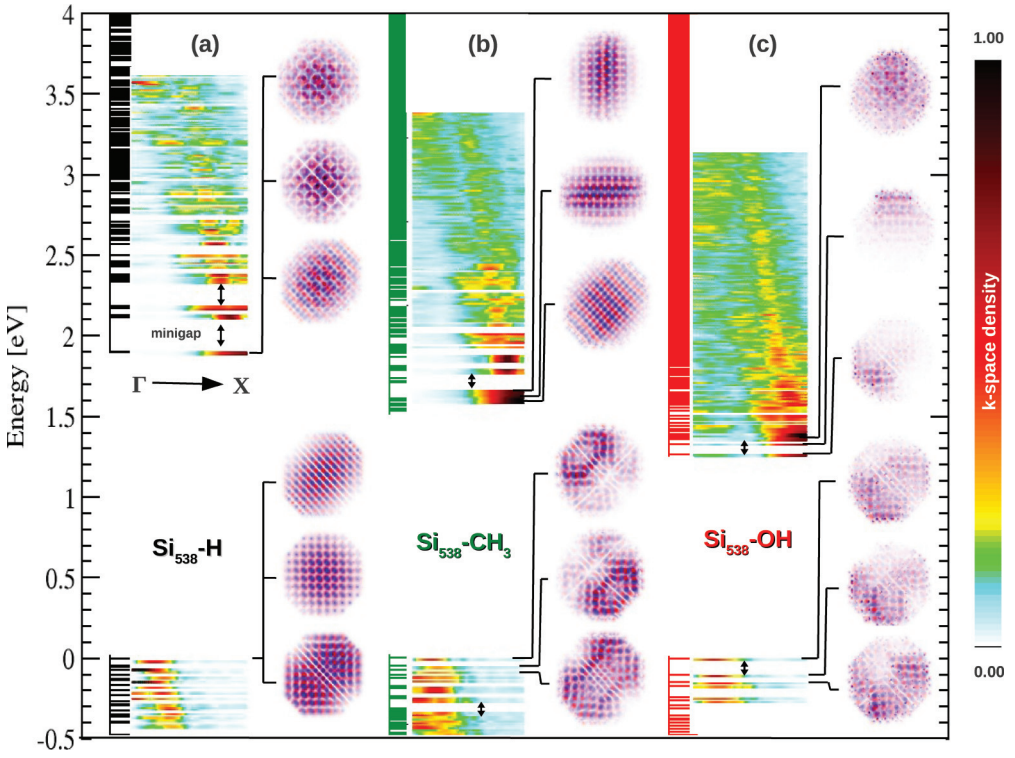

FIG. 10. (Color online) Spectrum of electronic states (black, green, and red bars) with their **k**-space projection from Γ to *X* (color scale legend, at the right) for (a) Si_{538}-H, (b) Si_{538}-CH_3, and (c) Si_{538}-OH. Real-space projections of selected frontier orbitals are plotted as well in order to show their overall shape, symmetry, and localization. Note: The color scale is limited to the same maximal value in order to enhance the contrast and to compare the absolute **k**-space densities between different passivations.

The calculated projected density of states for a Si_{538} NC is shown in Fig. 9(a). Surface states corresponding to Si-H bonds are localized far from the band-gap edges. Therefore, the highest occupied and lowest unoccupied electronic states are localized mainly in the core region. The electronic states in the Si NC core are strongly affected by the quantum confinement effect. Consequently, the band gap of a Si NC decreases with increasing NC diameter [see Fig. 9(d)], in good agreement with previous calculations.[26,28–30] We should note that band gaps in our calculations are underestimated due to the well-known DFT problem (see, e.g., Ref. 38).

Figure 10(a) displays real-space wave functions corresponding to individual electronic states at band-gap edges. We see that, in the case of hydrogen passivation, both HOMOs and LUMOs are spread almost homogeneously over the whole Si_{538} core. Applying our transformation method, we can convert electronic states from real to reciprocal space to obtain the electronic band-like picture of a Si NC with a given diameter. Figure 11 represents the projected **k**-space density along the Γ-*X* direction. We can see the gradual emergence of the fuzzy band structure with an increase in NC size. While for the smallest Si_{68} NC the band structure can hardly be recognized, in the case of the Si_{538} NC the dispersion of electronic states near the band gap mimics well the bulk band structure of both the conduction and the valence bands [compare Figs. 11(c) and 11(d)]. Therefore, we can estimate ≈2 nm to be a phenomenological limit where it makes sense to speak about the electronic fuzzy band structure and *indirect* band gap in silicon NCs. It is to be noted that a similar behavior was predicted for Si crystallite sizes lower than 2.5 nm in terms of enhanced efficiency of the radiative recombination rate.[23]

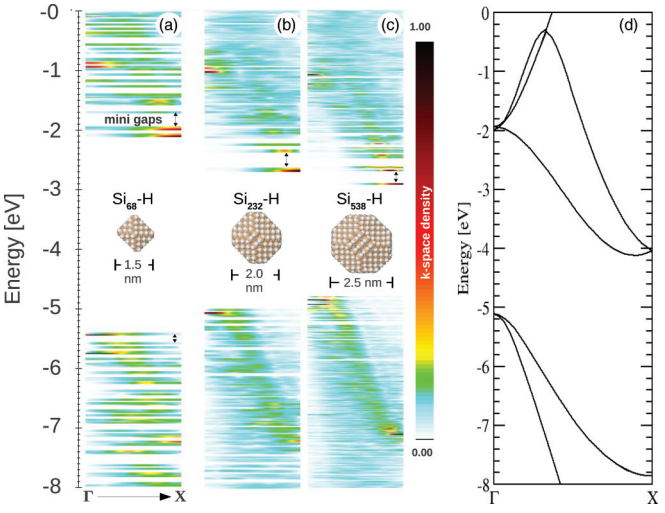

FIG. 11. (Color online) Comparisons of 1D cross sections of the projected **k**-space density in –H passivated NCs of different sizes for (a) Si_{68}-H, (b) Si_{232}-H, and (c) Si_{538}-H. Gradual emergence of energy bands can be seen with increasing NCsize. (d) Band structure of bulk Si for comparison. Note: The color scale is normalized by the maximal density independently for each NCsize.

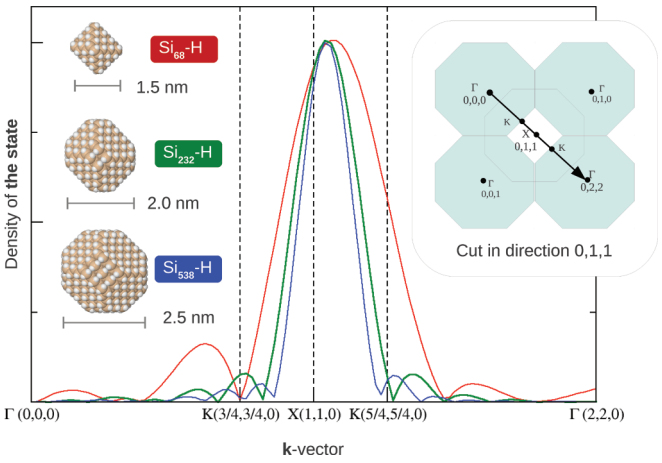

FIG. 12. (Color online) Delocalization of **k**-space projection of LUMO in –H passivated NCs depending on the nanocrystal diameter. The sinc-like shape can be clearly seen, which means an approximately rectangular envelope of the MO in real space.

There are two important differences between the bulk band structure and the projected band structure of a Si_{538}-H NC that must be noted: (i) the presence of discontinuities (minigaps) in the energy dispersion and (ii) delocalization (blurring) of electronic states in **k** space. The presence of the minigaps within the bands is induced by the finite size of the Si NC and the preserved symmetry of the atomic Si-core structure. The latter evokes the degeneracy of electronic states with a **k** vector in the equivalent crystal lattice directions in a manner similar to that shown in Fig. 8 for Si_{68}-H. We should note that the presence of minigaps larger the 63 meV can have important implications for the relaxation process of *hot* excited electrons from Γ to X. Usually, the maximal vibrational energy of phonons in bulk Si does not exceed 63 meV.[39] Therefore hot electrons might be unable to reach the conduction band minimum near X points once they meet the minigap along their path from Γ to X.

The blurring effect on electron states in momentum space can be directly attributed to the confinement in a finite space determined by the window function $w(r)$, as discussed in the previous section. Figure 12 shows the **k**-space density projection of the lowest unoccupied state onto a 1D line between the Γ(0, 0, 0) and the Γ(0, 2, 2) **k** points for different Si:H NC diameters. It demonstrates the variation of **k**-space delocalization and its shape depending on the size of the Si NC. We can clearly identify the sinc-like shape envelope corresponding to the rectangular step window function (see Fig. 6 for comparison).

B. SiNC:CH_3

In the next step, we examine an impact of the methyl ($–CH_3$) terminating group on the atomic and electronic structure of Si NCs. Our fully relaxed Si:CH_3 NCs expand by ≈1% of the lattice constant as a consequence of steric repulsion between the individual $–CH_3$ groups (see Fig. 14). The presence of mechanical strain causes inhomogeneities in the atomic Si-core structure, which lifts up the degeneracy of molecular states [see Fig. 10(b)]. This effect significantly reduces the size of the minigaps [see Fig. 10(b)]. Moreover, the electronic states are more localized in real space compared to those of a H-passivated NC of a similar size as shown by comparison of Figs. 10(a) and 10(b). Consequently, the *tails* of projected densities $\tilde{\rho}_i(\mathbf{k}')$ of individual electronic states in **k** space decay more slowly in **k** space than in Si:H NCs of the same size [compare again Figs. 10(a) and 10(b)]. This means that individual "bands" are not strictly localized in their **k** momentum.

We found out that the presence of nonpolar methyl groups leads to the localization of surface states in energies far from the Si NC band gap similarly to the situation in Si:H NCs [Fig. 9(b)], but the band gap is smaller compared to Si:H NCs [Fig. 9(d)].

C. SiNC:OH

According to our DFT simulations, Si NCs capped with hydroxyl (–OH) groups suffer from large atomic relaxation in proximity to the surface with respect to the Si bulk structure [see Fig. 14(c)]. Nevertheless, the atomic structure deep within the Si NC core remains almost intact and thus close to the bulk. The large distortion of the surface atomic structure is driven by the presence of significant charge transfer between Si and electronegative O atoms. The strong polarity of the Si-O bond tends to cause large localization of their MOs near the surface in real space [see Fig. 10(c)] with energies close to

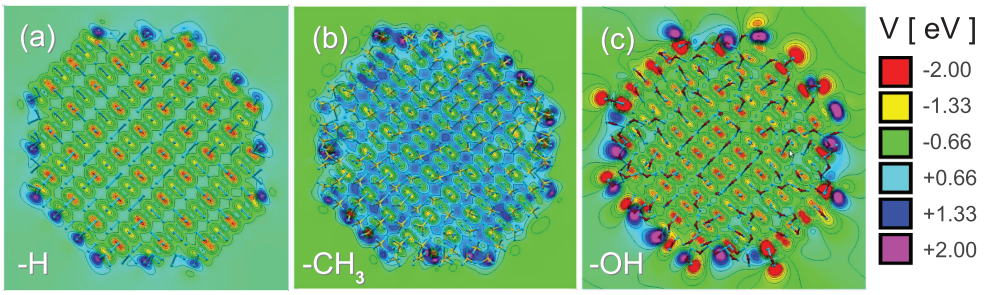

FIG. 13. (Color online) Map of Hartree potential inside Si_{538} NCs with different passivations. For nonpolar passivating groups (a) –H and (b) $–CH_3$, the potential is regular and corresponds to the charge distribution in the crystal lattice. However, for polar –OH passivation (c), a considerable number of local electrostatic fields can be seen near the surface. Note: The potential of neutral atoms was subtracted from the full self-consistent potential to make the features easily visible.

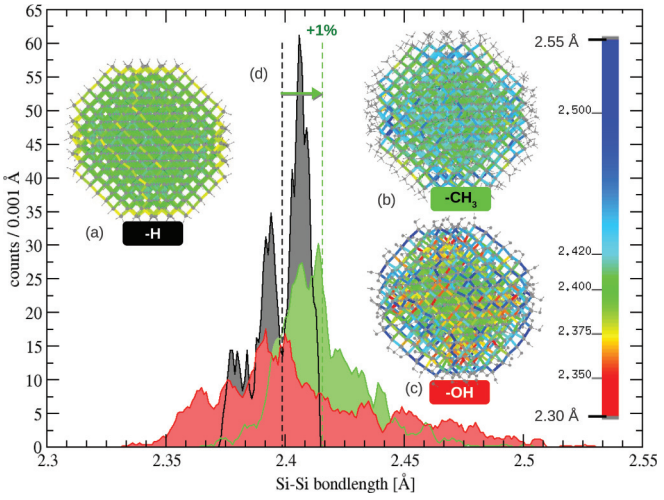

FIG. 14. (Color online) Histogram of Si-Si bond lengths in Si_{538} NCs with different passivations. Insets: Maps of bond length distortions in the color scale: (a) Si_{538}-H, (b) Si_{538}-CH_3, and (c) Si_{538}-OH. (d) Increase in mean bond length between –H and –CH_3 by 1%.

band-gap edges [Fig. 9(c)]. This picture is consistent with previous experimental evidence[40] and theoretical simulations[26–30] of oxidized Si NCs.

What is more, our simulations point out that –OH groups tend to align via hydrogen bonds, forming ordered domains at low temperatures. Consequently, considerable local electric fields are induced across the Si NC as shown in Fig. 13. We computed the electric dipole of 120 D for the largest –OH passivated NC (3 nm, Si_{538}), while the electric dipoles of the corresponding NCs passivated by –H (0.15 D) and –CH_3 (0.9 D) are negligible. The presence of the electric field together with the geometrical distortion of the surface layer [Fig. 14(c)] probably causes the irregular real-space distribution of HOMOs and LUMOs in –OH passivated NCs [Fig. 10(c)].

Due to the strongly localized states in the surface layer, the projected band structure is significantly blurred [with large *tails* of projected density $\tilde{\rho}_i(\mathbf{k}')$], which relaxes the **k**-space selection rules of optical transitions and improves the radiative recombination probability of *indirect* transitions. Also, the degeneracy of electronic states is almost removed due to the large distortion of atomic structure near the surface. This, however, goes hand in hand with the higher localization and irregular distribution of MOs in real space, which decreases the real-space overlap of orbitals and thus can limit the radiative recombination probability.

IV. DISCUSSION

In the previous sections, we have discussed the character of the fuzzy band structure of nanostructures depending on their size and surface passivation. We have shown differences with respect to the Si bulk band structure. First, utilization of the band-structure concept makes sense only for "larger" NCs, above a certain size limit. For example, for Si NCs this size limit lies between 1.5 and 2 nm (see Fig. 11), because under this limit the **k**-space projected MOs do not show much band-like behavior.

Second, the smaller the NC, the more pronounced the presence of minigaps inside the energy bands, which can limit the nonradiative relaxation of excitons. For the same size NCs, the minigaps are wider in more symmetric NCs with a weaker surface effect due to the degeneracy of energy levels (see Fig. 10).

Third, the nanoscale size introduces blurring of the **k** vector [see Figs. 12 and 4(d)]. Although this phenomenon is qualitatively easily predictable from the Heisenberg uncertainty principle and was already treated, e.g., by Hybertsen,[35] our approach allows us to quantify the influence of **k**-vector blurring for individual MOs.

Finally, in addition to describing the crystalline core, our computed band structures already include the effect of surface states. This is very important, because many types of real-life semiconductor NCs need to be capped by various surface terminating groups, which profoundly influences their electronic properties.

V. CONCLUSION

In this paper, we have introduced a general method to map effectively the electronic structure of aperiodic systems such as NCs from real space to reciprocal space. This method allows us to reassemble the fuzzy electronic band structure of finite-size systems. We believe that this method could provide more insight into the question whether the band-structure concept can still be applied to NCs of different shapes, sizes, or chemical compositions. In particular, we demonstrate that the fuzzy band-structure picture of nanometer-scale Si NCs can still be adopted down to a size of ≈2 nm, but with two important consequences of the finite size of the system: (i) the discretization and (ii) the delocalization of electronic states in the reciprocal space. This results also means that efficient slow red PL in Si NCs arises from indirect X-to-Γ electron-hole recombination, in agreement with recent experimental evidence.[41]

We employed this method to investigate the effect of Si NC size and the presence of different passivation groups including nonpolar and polar groups on their fuzzy band structure. We found that Si NCs capped with methyl groups expand by ∼1% due to steric repulsion between methyl surface groups. In the case of polar hydroxyl groups, real-space-localized states near the surface form band-gap edges, which tend toward rather delocalized **k**-space states. In other words, the band-structure concept is preserved, but near the band gap the electronic states become more blurred. In addition, we found strong alignment of hydroxyl groups forming a significant macroscopic electrostatic dipole moment across Si NC.

ACKNOWLEDGMENTS

We acknowledge Jan Valenta and Lubomír Skála for many useful discussions. This research was supported by the GACR 202/09/H041 project, GACR Centrum Excellence Grant No. P108/12/G108, and GAAV Grant No. M100101207.

*hapala@fzu.cz

[1] K. Brunner, U. Bockelmann, G. Abstreiter, M. Walther, G. Böhm, G. Tränkle, and G. Weimann, Phys. Rev. Lett. **69**, 3216 (1992).

[2] X. Sun, J. Liu, L. C. Kimerling, and J. Michel, Appl. Phys. Lett. **95**, 011911 (2009).

[3] J. Liu, X. Sun, D. Pan, X. Wang, L. C. Kimerling, T. L. Koch, and J. Michel, Opt. Express **15**, 11272 (2007).

[4] L. Nataraj, F. Xu, and S. G. Cloutier, Opt. Express **18**, 7085 (2010).

[5] L. Khriachtchev (ed.), *Silicon Nanophotonics–Basic Principles, Current Status and Perspectives* (Pan Stanford, Singapore, 2009), p. 472.

[6] V. Kumar (ed.), *Nanosilicon* (Elsevier, Amsterdam, 2008), p. 388.

[7] N. Koshida (ed.), *Device Applications of Silicon Nanocrystals and Nanostructures* (Springer Science & Business Media, New York, 2009), p. 360.

[8] L. Pavesi and R. Turan (eds.), *Silicon Nanocrystals: Fundamentals, Synthesis and Applications* (Wiley-VCH, Weinheim, 2010).

[9] L. Canham, Appl. Phys. Lett. **57**, 1046 (1990).

[10] L. Pavesi, L. D. Negro, L. Mazzoleni, G. Franzò, and F. Priolo, Nature **408**, 440 (2000).

[11] F. Trani, G. Cantele, D. Ninno, and G. Iadonisi, Phys. Rev. B **72**, 075423 (2005).

[12] P. Puschnig, S. Berkebile, A. J. Fleming, G. Koller, K. Emtsev, T. Seyller, J. D. Riley, C. Ambrosch-Draxl, F. P. Netzer, and M. G. Ramsey, Science **326**, 702 (2009).

[13] A. Valentin, J. Sée, S. Galdin-Retailleau, and P. Dollfus, J. Phys.: Condens. Matter **20**, 145213 (2008).

[14] X. Hu and J. Zi, J. Phys.: Condens. Matter **14**, L671 (2002).

[15] L. W. Wang, A. Franceschetti, and A. Zunger, Phys. Rev. Lett. **78**, 2819 (1997).

[16] Y. M. Niquet, C. Delerue, G. Allan, and M. Lannoo, Phys. Rev. B **62**, 5109 (2000).

[17] L. W. Wang and A. Zunger, J. Phys. Chem. **98**, 2158 (1994).

[18] L.-W. Wang and A. Zunger, Phys. Rev. Lett. **73**, 1039 (1994).

[19] T. Takagahara and K. Takeda, Phys. Rev. B **46**, 15578 (1992).

[20] F. Trani, D. Ninno, and G. Iadonisi, Phys. Rev. B **75**, 033312 (2007).

[21] A. S. Moskalenko, J. Berakdar, A. N. Poddubny, A. A. Prokofiev, I. N. Yassievich, and S. V. Goupalov, Phys. Rev. B **85**, 085432 (2012).

[22] A. N. Poddubny, A. A. Prokofiev, and I. N. Yassievich, Appl. Phys. Lett. **97**, 231116 (2010).

[23] C. Delerue, G. Allan, and M. Lannoo, Phys. Rev. B **48**, 11024 (1993).

[24] M. Lannoo, C. Delerue, and G. Allan, J. Lumin. **70**, 170 (1996).

[25] B. Delley and E. F. Steigmeier, Phys. Rev. B **47**, 1397 (1993).

[26] R. Guerra, E. Degoli, and S. Ossicini, Phys. Rev. B **80**, 155332 (2009).

[27] R. Guerra, E. Degoli, M. Marsili, O. Pulci, and S. Ossicini, Phys. Status Solidi (B) **247**, 2113 (2010).

[28] D. König, J. Rudd, M. A. Green, and G. Conibeer, Phys. Rev. B **78**, 035339 (2008).

[29] D. König, J. Rudd, G. Conibeer, and M. A. Green, Mater. Sci. Eng. B **159-160**, 117 (2009).

[30] K. Seino, F. Bechstedt, and P. Kroll, Phys. Rev. B **82**, 085320 (2010).

[31] J. P. Lewis, P. Jelínek, J. Ortega, A. A. Demkov, D. G. Trabada, B. Haycock, H. Wang, G. Adams, J. K. Tomfohr, E. Abad, H. Wang, and D. A. Drabold, physica status solidi (b) **248**, 1989 (2011).

[32] P. Jelínek, H. Wang, J. P. Lewis, O. F. Sankey, and J. Ortega, Phys. Rev. B **71**, 235101 (2005).

[33] M. Basanta, Y. Dappe, P. Jelinek, and J. Ortega, Comp. Mater. Sci. **39**, 759 (2007).

[34] F. Bloch, Z. Phys. **52**, 555 (1928).

[35] M. S. Hybertsen, Phys. Rev. Lett. **72**, 1514 (1994).

[36] D. Mariotti, S. Mitra, and V. Svrček, Nanoscale **5**, 1385 (2013).

[37] S. Ciampi, J. B. Harper, and J. J. Gooding, Chem. Soc. Rev. **39**, 2158 (2010).

[38] C. S. Wang and W. E. Pickett, Phys. Rev. Lett. **51**, 597 (1983).

[39] A. Dargys and J. Kundrotas, *Handbook on Physical Properties of Ge, Si, GaAs and InP* (Science and Encyclopedia, Vilnius, Lithuania, 1994), p. 264.

[40] M. V. Wolkin, J. Jorne, P. M. Fauchet, G. Allan, and C. Delerue, Phys. Rev. Lett. **82**, 197 (1999).

[41] D. C. Hannah, J. Yang, P. Podsiadlo, M. K. Y. Chan, A. Demortière, D. J. Gosztola, V. B. Prakapenka, G. C. Schatz, U. Kortshagen, and R. D. Schaller, Nano Lett. **12**, 4200 (2012).